J MATER SCI **41** (2006) 3987–3997

Microstructure and compressive properties of carbon microballoons

K. B. CARLISLE, M. KOOPMAN, K. K. CHAWLA, R. KULKARNI
Dept. of Materials Science & Engineering, University of Alabama at Birmingham, BEC 254, 1530 3rd Ave. S., Birmingham, AL, 35294-4461, USA

G. M. GLADYSZ, M. LEWIS
Los Alamos National Laboratory, Los Alamos, NM, 87545, USA

Published online: 7 June 2006

Carbon microballoons (CMBs) with tap densities of 0.143, 0.161, and 0.177 g/cm^3, as measured per ASTM B 527-93, were characterized in terms of individual balloon diameter, wall thickness, and mechanical behavior in compression through a novel uniaxial compression test technique. This compression test, performed on an MTS Nanoindenter XP II, utilized a flat-ended cylindrical tip rather than the common Berkovich indenter. Quantitative microscopy techniques were used to obtain diameter and wall thickness measurements on the polished cross-sections of individual CMBs that had been cold mounted in epoxy resin. Though there was significant overlap in the three populations, a trend toward increasing average wall thickness—from 1.32 to 2.16 μm—with increasing tap density was observed. Compressive property data including failure load, failure strain, fracture energy, and stiffness were obtained for individual microballoons. Comparison of these data, both inter- and intra-tap density, has yielded some viable trends. CMB failure strain exhibited a dependence upon the inverse square root of the CMB diameter, and CMB failure load depended linearly upon CMB stiffness. Averages for each tap density's failure load, pseudo-stiffness, and fracture energy were also calculated and observed to increase with tap density.

1. Introduction

Syntactic foams are a type of composite that is currently garnering considerable interest. In the increasing drive toward higher fuel efficiency, these foams are of especial importance. They provide a lightweight, high specific property component for composite beams and other structural applications in the transportation industry, and offer similar advantages to the aerospace and defense markets. In these foams, the voids are achieved by incorporating microballoons in the matrix thus utilizing the traditional blowing process only to produce the microballoons. Microballoons of ceramic, polymeric, or even metallic composition provide the voids through their geometry—namely a small, hollow, spherical shell. Syntactic foams currently exist in two basic varieties: two-phase and three-phase. The two-phase foams consist of microballoons in a continuous matrix material that completely occupies the space between them, whereas a three-phase foam has a polymeric matrix phase that does not completely occupy the voids between the microballoons. Multiphase foams merely build upon these two basic syntactic foams. Fig. 1 provides an example of a three-phase carbon microballoon (CMB) syntactic foam [1–3].

With research on the characterization and modeling of these foams intensifying, mechanical property data for the constituents becomes increasingly important. While data are often readily available for the binder phase, the same is not the case for the microballoons. Much of this inequity has stemmed from the lack of mechanical testing abilities for such small specimens; most microballoons used in syntactic foams are less than 500 μm in diameter, with many foams utilizing microballoons in the size range of 1–150 μm. Recent advances in materials testing equipment, combined with innovative adaptations, are allowing mechanical property information to be extracted from single microballoons.

There are several different material types of microballoons, as well as subcategories within each type, that may

0022-2461
DOI: 10.1007/s10853-006-7574-8

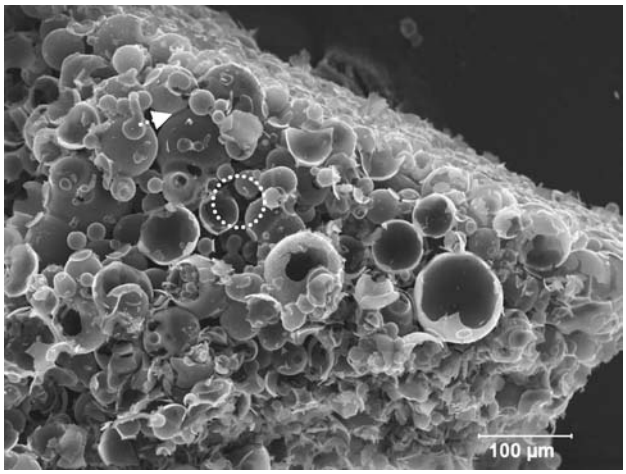

Figure 1 Micrograph of 3-phase CMB syntactic foam. SEM. Circle indicates intra-microballoon void region, and arrow points to APO-BMI between CMB.

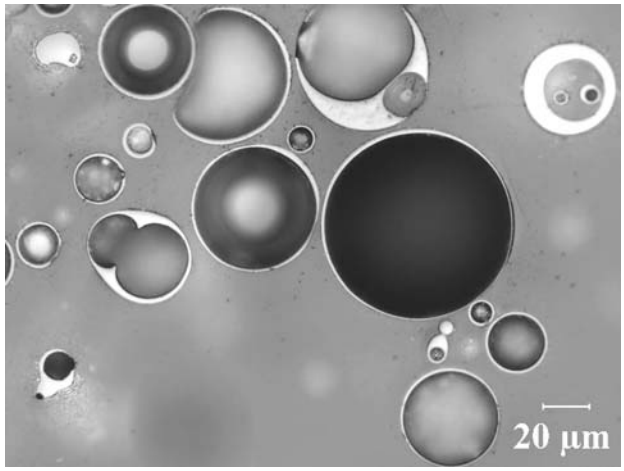

Figure 2 Polished cross-section of CMB mounted in epoxy. Image used for wall thickness measurements.

be used to construct syntactic foam. Glass and phenolic are two common materials in which microballoons are commercially available. Glass microballoons (GMBs) are often categorized according to size, wall thickness, and isostatic crush strength, thus providing some idea of their expected properties. However, this is not necessarily the case for other types of microballoons, including the carbon microballoons studied here. Instead, these CMBs are demarcated only by their tap density, an ASTM standard measurement (B 527) of the volume occupied by a known mass of powder after a suitable settling procedure. This test was originally intended as a measure of the bulk properties of metallic or ceramic powders, but it is now applied to microballoons. Tap density testing provides a measure of the average wall thickness of a particular test lot, assuming that each lot has similar settling behavior, but yields no indication of individual microballoon properties [4–7].

2. Experimental procedures

2.1. Quantitative microscopy

Determination of microballoon size and wall thickness complements the data from compressive testing. The original problem of examining the CMBs was that of obtaining proper cross-sectional images. This was solved by developing a unique polishing procedure for use with the highly porous CMB foam [5]. Further adaptation of this technique has led to the mounting of CMBs in epoxy resin, and subsequent polishing. Note that most CMBs, when mixed with epoxy for mounting, float. This difficulty was alleviated by double mounting the specimens. First, CMBs were mixed into resin, which hardened with most CMBs rising to the top surface of the mount. These mounts were then sectioned using a diamond wafering saw and re-mounted in epoxy at an orientation perpendicular to the original mounting orientation. This allowed polishing through a cross-section of the CMB-rich surface layer of the original mount. Random optical images (see Fig. 2) of this surface were then taken at 500 X magnification, and the minimum and maximum diameter and wall thickness of each single walled microballoon were measured. It must be recognized that these measurements are mean lineal intercepts (λ) and not direct measures of wall thickness or diameter because the location of the sectioning plane through each microballoon is unknown. If the balloon were sectioned along its great circle, then the measurements would be the actual diameter (ϕ) and thickness (t); however, if the sectioning plane lay above or below a great circle, as illustrated in Fig. 3, the measured diameters will be less than the actual diameter and the measured intercept through the wall will exceed the actual radial measure. Since the location of the sectioning plane of each CMB was unknown, statistical methods were applied to the mean lineal intercept measurements, providing the calculated diameter or wall thickness. The formula relating the mean lineal intercept ($\lambda_{diameter}$) through a spherical object to the diameter (ϕ) is [8]

$$\phi = \left(\frac{3}{2}\right)\lambda_{diameter} \tag{1}$$

Starting from the definition of the mean lineal intercept, which states that the intercept is four times the volume divided by the surface area per unit volume [7], and the geometric relationship between the internal diameter, external diameter, and thickness of a spherical shell, the wall thickness can be related to the actual diameter and measured mean lineal intercept:

$$\bar{\lambda}_{wall} = \frac{4t(t^2 - 1.5t\phi + 0.75\phi^2)}{3(t^2 - t\phi + 0.5\phi^2)} \tag{2}$$

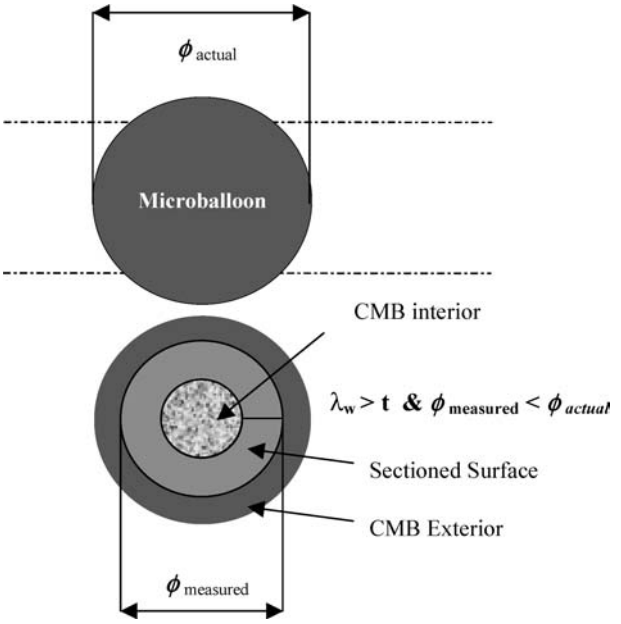

Figure 3 Schematic illustrating sectioning a CMB either below or above its great circle (dashed lines). Note that measurements made on the section will be inaccurate due to the curvature of the CMB.

Equation 2 was solved for each measured CMB, using that particular CMB's corrected diameter and mean lineal intercept. These data have been used to calculate average thickness for each tap density, in addition to obtaining individual thickness vs. diameter graphs.

2.2. Compression testing of individual microballoons

Three lots of carbon microballoons were selected for this study. They are distinguished by tap density; approximately 140 CMBs from each 0.143, 0.161, and 0.177 g/cm^3 tap density lot were subjected to uniaxial compression testing, on a micrometer-level scale. Although this procedure has been delineated in detail elsewhere [4], a brief description will be presented here. A Nanoindenter XP II by MTS Nano was adapted to take advantage of its 0.02 nm displacement resolution and 50 nN load resolution to perform the compression test. In this endeavor, a polished Al substrate is inserted into the indenter's specimen stage, and a flat-ended sapphire tip is substituted for the typical Berkovich indenter. These two surfaces become the lower and upper platens, respectively, for the ensuing compression of individual microballoons that were carefully placed on the Al surface prior to testing. A schematic representation of this apparatus is shown in Fig. 4. The load cell and *x*-*y* planar movement of the instrument were calibrated via the traditional techniques prior to testing, ensuring both the accuracy of measurement and the uniaxiality of the test. These compressive tests yielded very accurate load and platen displacement

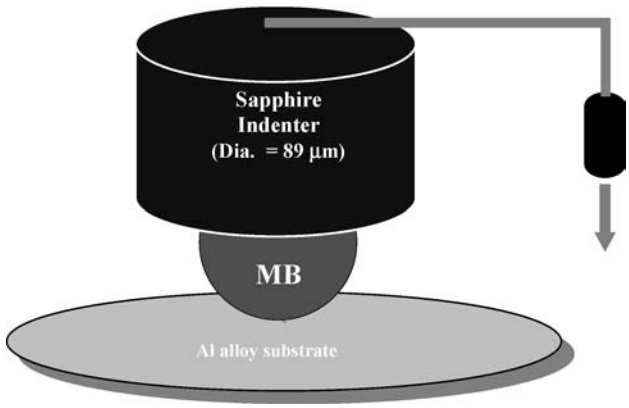

Figure 4 Schematic of nanoindenter modified for use in compression testing of CMB. Cylinder at right represent attached optical microscope.

data for the compression of individual CMBs from each tap density, as well as a measurement on the *x*-*y* plane of the CMB's diameter (ϕ_h) via the attached optical microscope.

Failure loads (P_f) for each CMB were obtained by this test. Careful consideration of the test geometry also indicates that the displacement data yielded an accurate measure of the diameter (ϕ_v) of each CMB—it was the total distance traveled by the sapphire indenter from initial contact with the microballoon until contact with the Al substrate. Note that the subscript v indicates that ϕ_v is what we term the vertical diameter, which, due to the imperfectly spherical nature of the CMBs, may not exactly equal the horizontal diameter measurement. The failure point also provided the displacement at failure (δ_f), which was used in conjunction with the diameter to define the failure strain (ε_c) of each CMB as follows:

$$\varepsilon_c = \left(\frac{\delta_f}{\phi_v}\right) \tag{3}$$

The linear loading segment is characterized by a pseudo-stiffness (k) of the CMB. This is essentially a spring constant term, and is presumably a function of: the modulus of the carbon in the CMB's walls, the CMB's diameter, the CMB's wall thickness, and the CMB's concentricity. Another useful parameter defined from the load-displacement curve was the work of fracture (W_f) for the microballoon:

$$W_f = \frac{1}{2} P_f \delta_f \tag{4}$$

This term is obtained as illustrated in Fig. 5 for single-wall CMBs, but is actually the sum of several such triangular or trapezoidal areas for CMBs of more complicated morphology. The work of fracture can also be predicted from the shell theory case of concentrated uniaxial compressive loading. The expression for the work of fracture in terms of the properties obtainable from compression testing (P_f

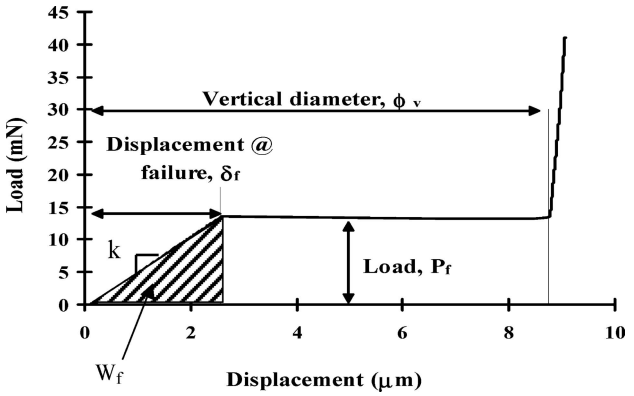

Figure 5 Sample compression curve for a single wall CMB, showing parameters extracted from graph.

and ϕ_v) is,

$$W_f = \frac{AP_f^2\phi_v\sqrt{1-\nu^2}}{4Et^2} \tag{5}$$

where the Young's Modulus (E) of the CMB wall material was selected as 12 GPa (reasonable based on nanoindentation), Poisson's ratio (ν) was chosen as 0.22 (valid for this type of carbon), and A is a tabulated coefficient that varies from 0.433 to 0.286, depending on the MB to platen contact area and the MB's diameter [9]. The wall thickness used was the average calculated value for each tap density.

3. Results

3.1. CMB morphology

The initial assumption was that a microballoon was a spherical shell of essentially constant wall thickness; however, the actual structure of these CMBs is much more irregular. Fig. 6, a scanning electron microscope (SEM) image, shows that while many of the CMBs are indeed roughly spherical, there are also many complicated, non-spherical shapes. Note the conjoined (circled region) and broken (arrow) CMBs in the micrograph. These can certainly not be approximated as a spherical shell. Cross-sectional images revealed many other issues, the two most detrimental of which are significant wall thickness variations and the presence of multi-compartmented interiors, i.e., nested CMBs, see Fig. 7.

Based on the microstructures of the CMBs shown above, it is obvious that there should be large differences in mechanical response based on the CMB's morphology. Therefore, the CMBs have been classified as either single walled (SW) or nested (N). These two types of CMB do indeed possess distinctive loading behavior, as can be seen in Fig. 8 [5]. A third category is also presented. The behavior of these flawed-single walled (FSW) CMBs falls between that of the other two types; there is a single loading region that has a non-linear nature. The flawed-single-walled CMB category has been observed consistently and is thought to be the result of CMBs that have either surface irregularities or defects within their walls.

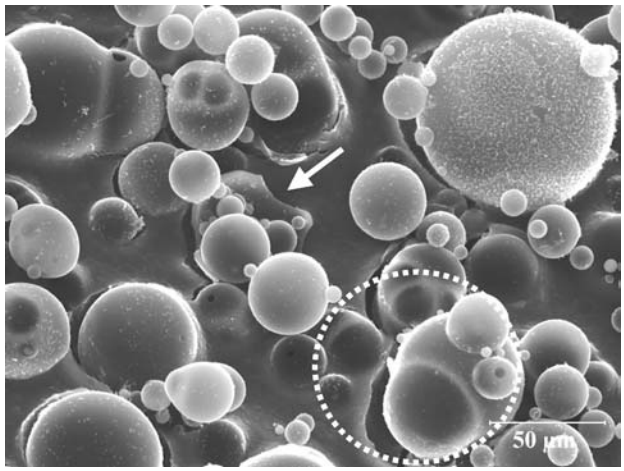

Figure 6 Micrograph showing variation in CMB size and morphology. Broken (arrow) and conjoined (circle) CMBs visible. SEM.

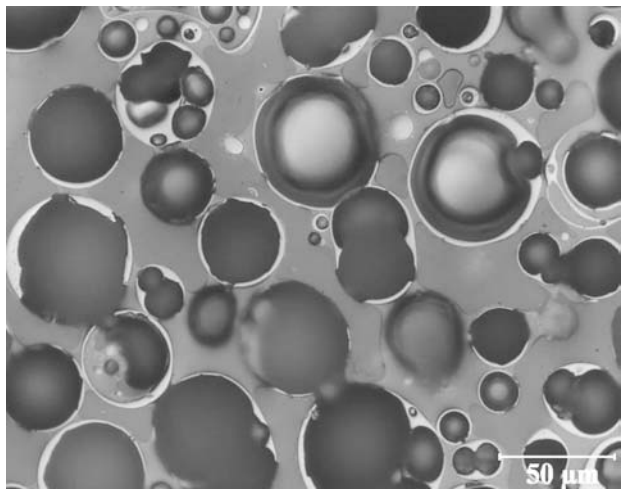

Figure 7 Polished cross-section of CMB foam. Note the interior compartments, wall thickness imperfections, etc.

3.2. Wall thickness and diameter

Statistically valid quantitative microscopy formulae (Equations 1 and 2) were applied to mean lineal intercept data on wall thickness and diameter from individual CMB of each tap density to yield calculated thickness and diameter. The wall thickness vs. diameter for similar population sizes from each tap density is plotted in Fig. 9. Additionally, overall average wall thickness and its standard deviation were calculated within each tap density lot. These are shown in Fig. 10, demonstrating the trend toward increasing average wall thickness with increasing tap density.

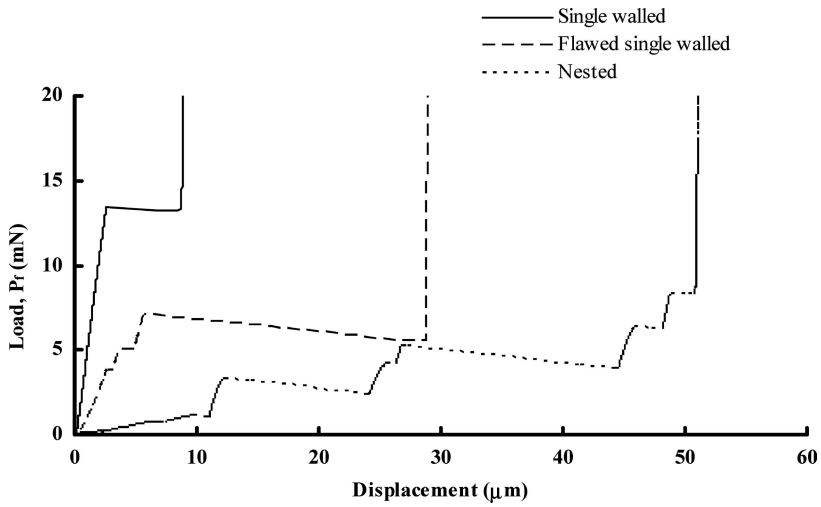

Figure 8 Examples of different CMB compressive behavior based on CMB morphology [5].

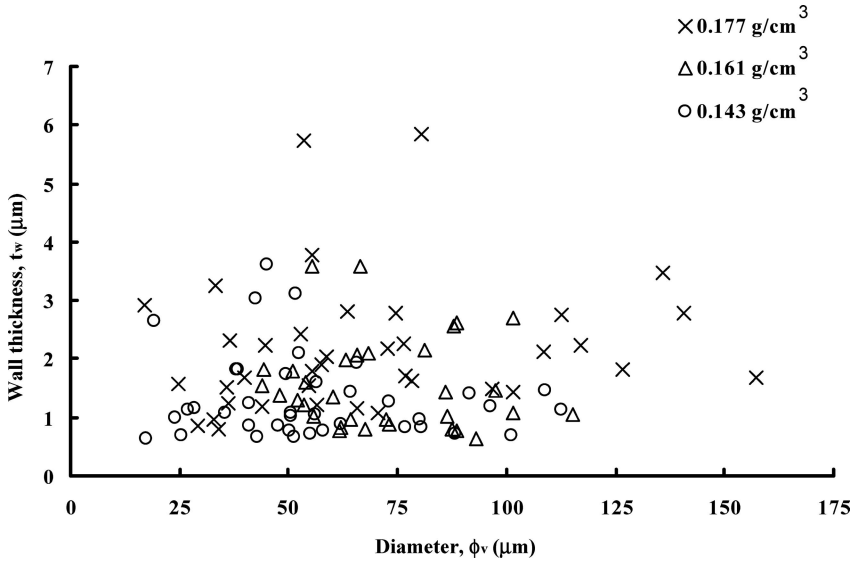

Figure 9 CMB diameter vs. wall thickness. No observable correlation. All values were corrected to reflect the CMB's 3D geometry.

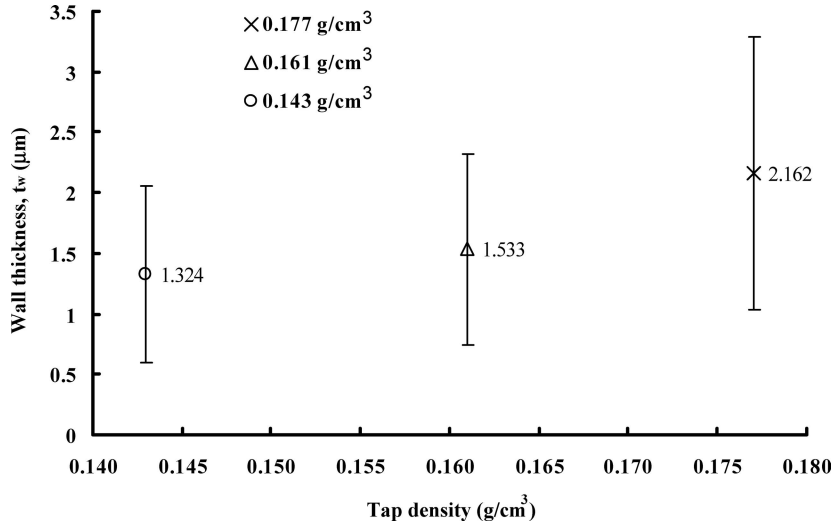

Figure 10 Calculated average CMB wall thickness vs. tap density. Trend toward increasing average wall thickness with higher tap density is apparent.

3.3. Compression of single CMBs

The data collected from the compression curves of individual CMBs were tabulated for each tap density. Averages and standard deviations were calculated for failure load, pseudo-stiffness, and work of fracture for each of the three categories of CMB. Table I provides a comparison of these properties. Fig. 11 provides clarification for the sub-categories, showing the initial and ultimate properties in the schematic. Some explanation is required for the case of the ultimate fracture energy. As with the single-walled CMBs, this is calculated as the area under the load-displacement curve, except that a nested curve proceeds in a discontinuous fashion, with at least two regions where the indenter tip is merely traveling downward until it meets a subsequent internal compartment. Assuming that the initial compartment is structurally connected to internal compartments for the majority of nested CMBs and all compartments begin loading concurrently, the work of fracture (W_f) is calculated as the sum of an initial triangular area and the subsequent trapezoidal regions.

Since trends beyond average properties were expected, several of the compressive properties have been plotted against CMB size and one another, with the relevant graphs presented in the figures that follow. The diameter vs. work of fracture curve exhibited low R^2 values in the regression analysis, but when plotted co-axially with estimated fracture energies calculated from experimental load and CMB diameter using Equation 5, good agreement between the calculated and fitted curves was observed [9]. Then, it was apparent that the trend in Fig. 12 was of some significance despite the minimal dependence on CMB diameter. Equation 5 was also used to calculate predicted effective wall thickness, using measured work of fracture (Fig. 13). One of the two other trends that became apparent was that of compressive strain vs. diameter, shown in Fig. 14. This trend is evident across all CMB tap densities tested. Fig. 15 shows failure load vs. pseudo-stiffness, with a linear fit for each tap density yielding improved correlation.

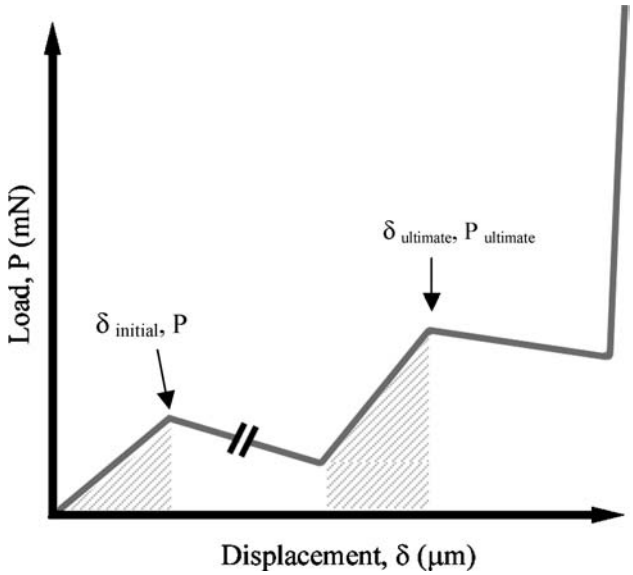

Figure 11 Schematic representation of nested compression curve, with initial and ultimate properties labeled. The gray shading represents the work of fracture for a nested CMB.

4. Discussion

Preliminary testing of this foam material has shown that, at constant volume fraction, increasing the tap density of the constituent CMBs did improve the overall compressive strength and modulus of the composite foam [10]. It was expected that this trend would continue in the CMBs themselves, with higher tap densities displaying greater load bearing ability, as well as increased stiffness. Additionally, CMB size was expected to affect failure loads. However, due to extreme irregularity in the microballoons and the inability to determine actual wall thickness of the individual MB tested, failure stresses for the CMBs could not be determined; thus, with the trend of CMB diameter vs. failure load proving tenuous, average failure loads must suffice as a measure of CMB strength. To a small degree, the evidence in Table I regarding single-walled microballoons does support the hypothesis of better CMB properties with increasing tap density. However, although the average load at failure, with values of 11.4, 12.9, and 14.6 mN for the 0.143, 0.161, and 0.177 g/cm^3 CMBs respectively, does display a positive correlation with tap density, the overlap in the data prevents the relationship from being statistically significant on a 95% confidence level. Pseudo-stiffness also exhibited increasing average values with increasing tap density. In this case, the 0.143 and 0.161 g/cm^3 tap densities are both statistically

TABLE I Average properties of CMB by category

CMB category		SW			FSW			N	
Tap Density (g/cm^3)	0.143	0.161	0.177	0.143	0.161	0.177	0.143	0.161	0.177
$P_{f\ ultimate}$ (mN)	11.4	12.9	14.6	11.6	11.3	10.9	8.0	10.7	12.8
$P_{f\ initial}$ (mN)		NA			NA		2.7	3.1	3.9
$W_{f\ total}$ (nJ)	22.2	29.6	27.5	37.3	29.9	35.2	23.4	19.9	24.1
$W_{f\ initial}$ (nJ)		NA			NA		6.3	5.4	8.2
$k_{average}$ (kN/m)	3.5	3.6	4.7	2.1	2.6	2.0	1.9	3.1	3.5
$k_{initial}$ (kN/m)		NA			NA		0.8	1.2	1.1

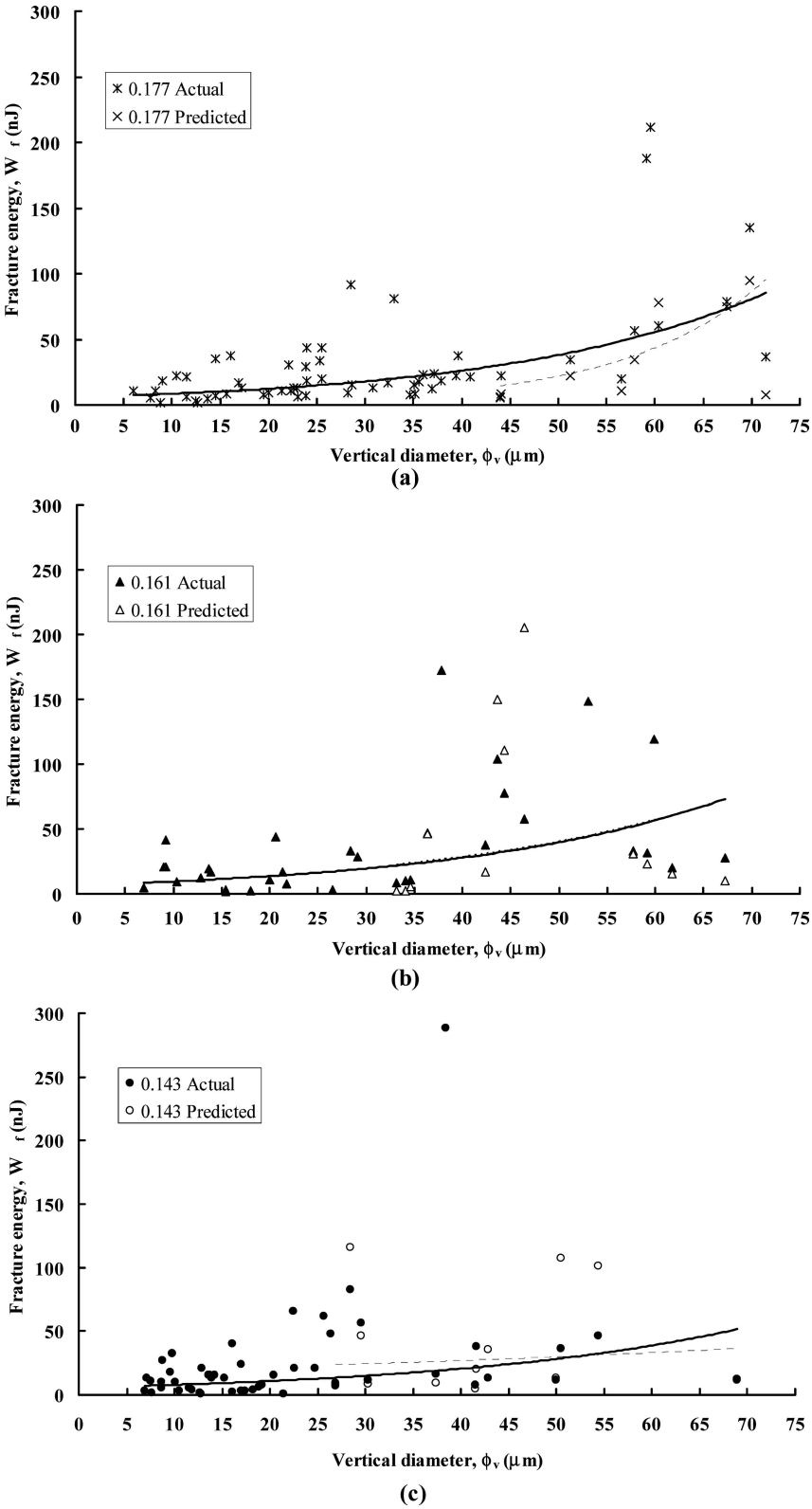

Figure 12 Fracture energy vs. diameter for single wall CMBs, with bold lines for experimental and thin lines for calculated trends. Units in the inset are g/cm^3. Experimental curves are shown only in the region where R/t > 10 and Equation 5 applies. (a) 0.177 g/cm^3 tap density CMBs. (b) 0.161 g/cm^3 CMBs. Experimental and theoretical curves overlap in the figure. (c) 0.143 g/cm^3 CMBs.

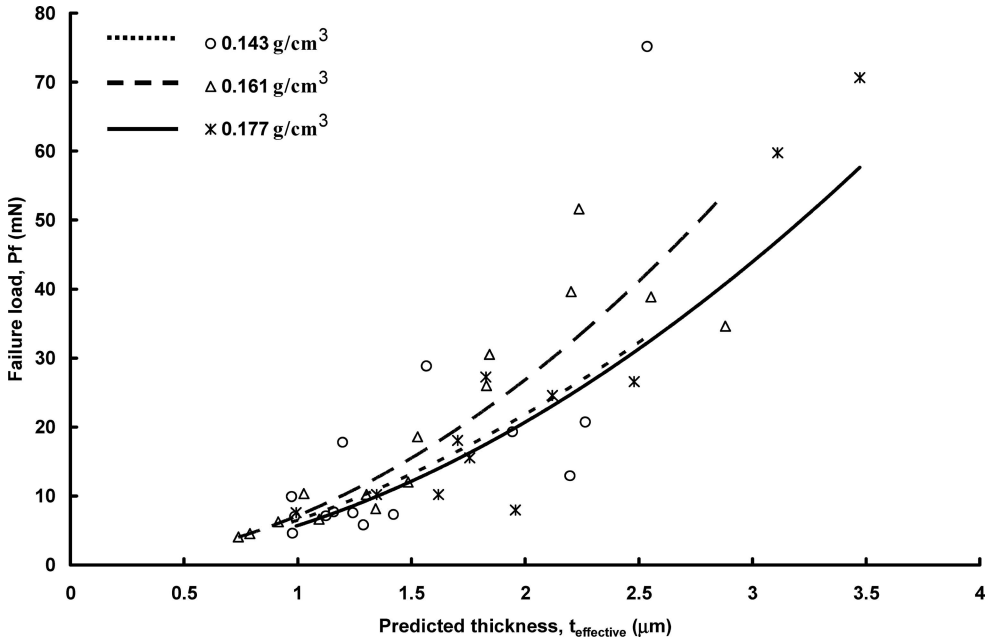

Figure 13 Failure load vs. predicted thickness for single walled CMBs, revealing a parabolic dependence of failure load on thickness.

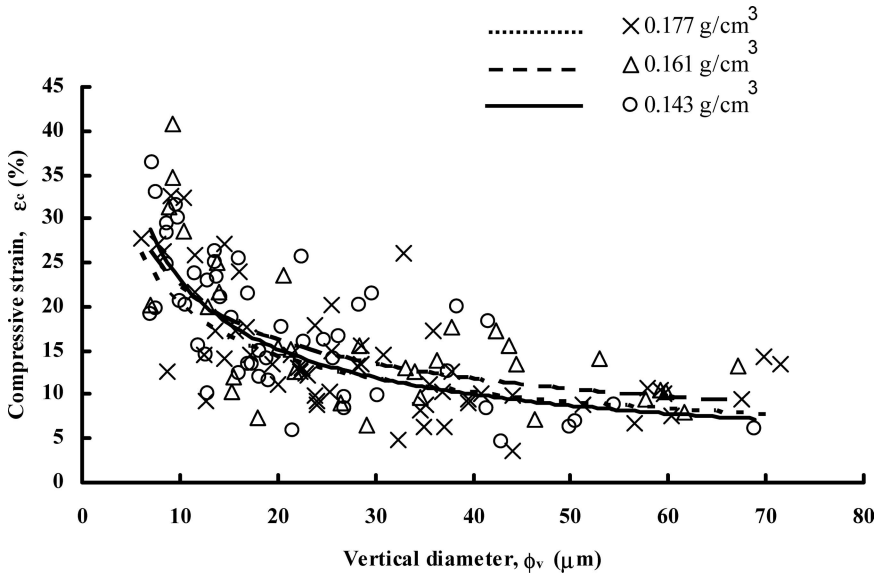

Figure 14 Compressive strain trend for single wall CMBs. Trend appears similar for all tap densities.

different from the 0.177 g/cm^3 CMBs, although they themselves will not pass a *t*-test as different populations. Unfortunately, the average work of fracture values, which also show general increases with increasing tap density, cannot be shown to be of statistically significant difference at the 95% confidence level. Thus far, the average property data have only demonstrated that there are small differences in properties with tap density, most of which cannot be statistically verified. When the flawed-single-walled and nested CMB data in Table I are analyzed, it quickly becomes apparent that these types of CMBs follow the same trends as do the single-walled CMBs, with the noted exception that nested CMBs have significantly lower average failure loads and pseudo-stiffnesses. Doubtless this inferiority was due to the much higher incidence of thin regions and other flaws in their walls, as can be easily observed in Figs. 2 and 7. Further investigation into the average properties of the flawed-single-walled CMBs and nested CMBs showed that the tap densities cannot be proven to be statistically separate in any average property category except pseudo-stiffness, which showed the same differentiation between the lowest two tap densities and the highest tap density that was exhibited by the single walled CMBs.

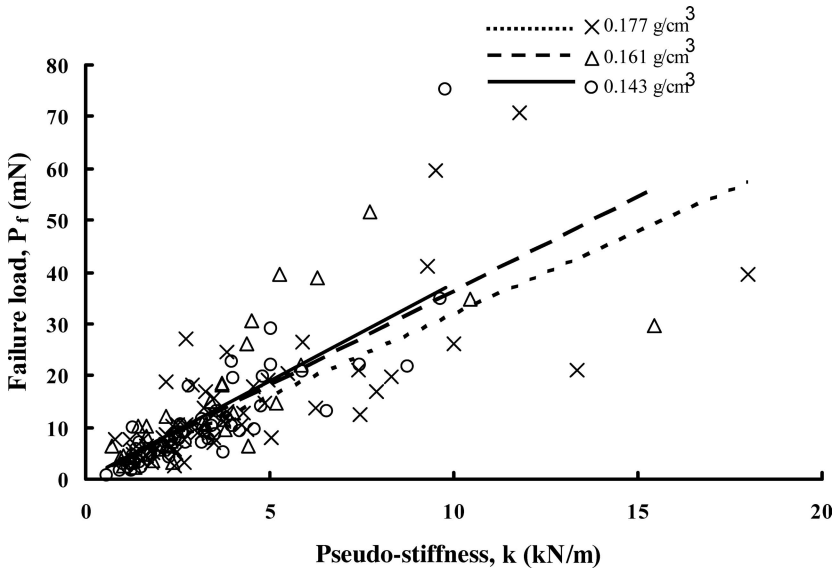

Figure 15 Load vs. Pseudo-stiffness trend for all tap density single wall CMB.

Fig. 12 shows one of the least viable trends, work of fracture vs. diameter for single-walled CMBs. In this figure, the bold lines represent the experimental data and the thin lines show the calculated work of fracture, from Equation 5 using measured failure load, diameter, and average wall thickness. Even though the experimental curves have poor fit coefficients, this correlation well represented the average behavior of a CMB of a particular diameter and, as can be seen by the parity in the experimental and calculated curves, is accurately predicted by the theoretical model for a spherical shell under a concentrated uniaxial compressive load. In order to obtain the predicted values, we assumed point contact in the use of the tabulated numerical coefficient (A), and it would yield better agreement with the experimental data if the contact area of the concentrated load were allowed to become a small area of radius less than 5 μm. However, since the actual contact area is unknown and would vary with both CMB wall thickness and diameter, only the simplest case has been presented in Fig. 12. Despite this simplification, the predicted fracture energy agrees so well with the experimental that the two trend curves actually overlap for the 0.161 g/cm^3 tap density. Given that in the model we used actual load and diameter in addition to the average wall thickness of the CMBs in a particular tap density, this agreement between the theoretical and experimental data provides evidence related to the cause of the variation in experimentally observed fracture energies. The experimental trend line represents the average behavior of all of the CMBs tested in compression; since this trend followed the theoretical behavior of a CMB having the average wall thickness of that tap density, it is thought that wall thickness variations above or below the average used in the model are the cause of the wide scatter in the experimental data. Thus, the theoretical model could be used to predict an accurate and valid average work of fracture for a particular tap density CMB, having measured average load, diameter, and wall thickness. Conversely, the effective thickness of a CMB with measured load, diameter, and work of fracture could be predicted by the model, as in Fig. 13.

Fig. 14 shows compressive strain at failure of the single-walled CMBs is proportional to the inverse square root of CMB diameter, a trend that has been observed in the three tap density CMBs tested in this study, and in other CMBs previously tested [5]. Given the behavior of the trend lines, it is concluded that this trend is valid for all single-walled CMBs and is essentially independent of tap density. Comparison with research on glass microballoons reveals that this trend may be unique to CMBs, since it has not been observed in other systems [4, 11]. The fact that there is no observed trend in wall thickness with CMB diameter (Fig. 9) means that small and large CMBs have similar wall thicknesses; and hence, the small CMBs contain less volume of carbon in their walls. This reduction in available carbon wall material in smaller diameter CMBs is speculated to limit the maximum flaw size in the CMB, as shown in Fig. 16. The classic argument for a brittle material following Weibull statistics means that there is a reduced probability of finding a critical flaw size in a smaller CMB due to its lesser volume. This, when applied to the compressive strain results, explains the failure of smaller diameter CMBs at higher strains (and hence greater strengths). Additionally, the location, relative to the compression platens, of a flaw like that depicted in Fig. 16 is expected to affect the compressive strengths of the CMBs.

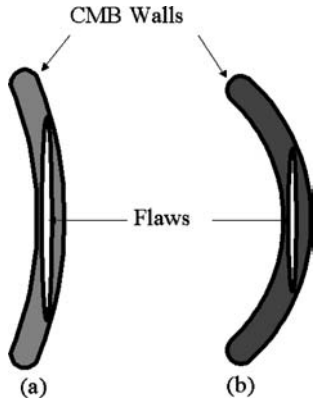

Figure 16 Schematic of speculated flaw size limitations in smaller diameter CMBs. CMBs in (a) and (b) are of identical thickness, with shell (a) having twice the diameter of (b). The smaller maximum flaw size for the smaller CMB is clearly shown.

However, since flaw location is unknown experimentally, the exact effect on the compressive data cannot be determined.

Fig. 10 shows the general increase in average wall thickness with tap density. Here, the 0.143 g/cm^3 CMBs and the 0.161 g/cm^3 CMBs cannot be considered to be statistically different populations at the 95% confidence level, but the 0.177 g/cm^3 tap density average thickness tested as significantly different at the same significance level. Recall that average pseudo-stiffness for single-walled CMBs also showed little difference between the lower two tap densities but clearly separated the highest tap density. Now, an overall trend emerges connecting wall thickness and pseudo-stiffness. If a microballoon during compression were considered to be essentially a spring, its k value would depend on the inherent stiffness of the material and the spring geometry. For a metal coil spring, this would be the coil size, wire diameter, and wire cross-section. For a microballoon, the important geometrical parameters are diameter (ϕ) and wall thickness (t). The higher average thickness results in greater stiffness for the 0.177 g/cm^3 tap density. Further evidence of the effect of thickness on mechanical properties is observed in Fig. 15. It shows that, within any tap density, CMBs of higher stiffness also possessed greater failure loads. Additionally, inter-tap density comparison showed that the highest tap density had a clearly greater stiffness at any given load, as expected given its higher wall thickness. This emphasis on wall thickness controlling failure properties corresponds well to previous studies. Bratt *et al*. [11] showed that the uniaxial compressive failure load of a glass microballoon was independent of its diameter and related only to the average strength and wall thickness squared of the MB, a similar result to that seen in Fig. 13 relating CMB failure load to predicted wall thickness. Their exclusive focus on GMBs, where the wall thickness and single-walled nature of each GMB were determined by means of an interference microscope prior to testing, prohibits further comparison to the CMB work presented here, due to the opaque nature of the CMBs.

5. Conclusions

Through the novel use of a modified nanoindenter, in this work we have tested carbon microballoons of three different ASTM B527 tap densities in uniaxial compression. Optical and scanning electron microscopy of these CMBs has shown the existence of several morphologies, including single-walled and nested CMBs. Additionally, microscopic techniques have proven that the highest tap density possessed thicker walls than the other two tap density CMBs.

A statistical approach to the data presented several trends. Compressive strain was proportional to the inverse square root of diameter for all tap densities; failure load was seen to correlate linearly with stiffness; and fracture energy was observed to have some small dependence on diameter that was readily predictable via theoretical formulas. Average failure load, fracture energy, and pseudo-stiffness from the CMBs showed increases with increasing tap density, although these differences were not always statistically significant. Additionally, single-walled CMBs exhibited superior average failure loads, fracture energies, and pseudo-stiffnesses than nested CMBs. Although the correlation between wall thickness and tap density did elucidate most of the trend toward increasing mechanical properties, research into other possible explanations is still ongoing.

Acknowledgments

This work was financially supported by Los Alamos National Laboratory/DOE subcontract #44277-SOL—02 4X

References

1. K. OKUNO and R. R. WOODHAMS, *Cell. Plast.* (1973) 8.
2. H. S. KIM and H. H. OH, *Applied Polymer Science* **76**(2000) 1324 5.
3. G. GLADYSZ and K. K. CHAWLA, in "Composite Foams, in Encyclopedia of Polymer Science & Technology" (John Wiley, New York, 2004) p. 267.
4. M. KOOPMAN, G. GOUADEC, K. CARLISLE, K. K. CHAWLA and G. GLADYSZ, *Scripta Materialia* **50** (2004) 593.
5. K. CARLISLE, K. K. CHAWLA, G. GOUADEC, M. KOOPMAN and G. M. GLADYSZ, in Nanocompressive properties of carbon microballoons and mechanical properties of carbon based syntactic foam composites. in ICCM-14 (San Diego, CA, 2003) Society of Manufacturing Engineers.
6. ASTM D 3102-78: Standard Practice for the Determination of Isostatic Collapse Strength of Hollow Glass Microspheres. American Society for Testing and Materials. (1984).
7. K. CARLISLE, K. K. CHAWLA, G. GLADYSZ and M. KOOPMAN, *J. Mat. Sci.* (2006) (this issue).
8. R. T. DEHOFF and F. N. RHINES (Eds.), in "Quantitative Microscopy" (McGraw-Hill, New York, 1968).

9. R. J. ROARK, in Roark's Formulas for Stress and Strain edited by W. C. Young (New York: McGraw-Hill, 1989)p. 542.
10. G. M. GLADYSZ, B. PERRY, G. MCEACHEN and J. LULA, *J. Mat. Sci.* (2006) (This issue).
11. P. W. BRATT, J. P. CUNNION and B. D. SPIVAK, in Mechanical Testing of Glass Hollow Microspheres, in Advances in Materials Characterization edited by D. R. Rossington, R. A. Condrate and R. L. Snyder (New York, Plenum Press, 1983) p. 441.